Scripta Materialia 110 (2016) 82–86

Contents lists available at ScienceDirect

Scripta Materialia

journal homepage: www.elsevier.com/locate/scriptamat

Adjustable dielectric properties of $BaTiO_3$ containing MgO inclusions deformable under Spark Plasma Sintering

Romain Epherre [a,b], Julien Lesseur [c,d], Marjorie Albino [c,d], Philippe Veber [c,d], Alicia Weibel [a,b], Geoffroy Chevallier [a,b], Mario Maglione [c,d], Dominique Bernard [c,d], Catherine Elissalde [c,d], Claude Estournès [a,b,*]

[a] CNRS, Institut Carnot Cirimat, F-31062 Toulouse, France
[b] Université de Toulouse, UPS, INP, Institut Carnot Cirimat, F-31062 Toulouse, France
[c] CNRS, ICMCB, UPR 9048, F-33600 Pessac, France
[d] Université de Bordeaux, ICMCB, UPR 9048, F-33600 Pessac, France

ARTICLE INFO

Article history:
Received 18 June 2015
Accepted 9 August 2015
Available online 24 August 2015

Keywords:
Nanocomposite
SPS
Sintering
$BaTiO_3$
Dielectric properties

ABSTRACT

Spark Plasma Sintering (SPS) is an efficient technique to produce highly densified ferroelectric–dielectric composites with good control of the interfaces and microstructures. We present an effective approach based on precursor preparation to produce $BaTiO_3$/MgO with adjustable hardness for the inclusions. The influence of their rigidity on the sintering composites was investigated and the possibility of being able to tailor the permittivity simply by changing the morphology of the MgO inclusions was demonstrated.

During the last decades considerable efforts have been made regarding the synthesis and production of structural and functional nanocomposites. These materials have been widely explored for many technological applications because they exhibit enhanced mechanical, magnetic, optical, or catalytic properties which cannot be achieved with single materials [1]. In the field of electronics and telecommunications, many research programs have focused on nanocomposites composed of $Ba_{1-x}Sr_xTiO_3$ (BST) matrix with $x = 0$ to 1 in which metallic [2,3], polymer [4,5], and ceramic inclusions were added [6,7]. In these works, three issues systematically recur: (i) avoiding interdiffusion and controlling the interfaces; (ii) optimizing inclusion morphology and the sintering behavior of two different materials; (iii) managing the synergy of the final properties.

In these papers focus is given on the preparation of composites mixing ferroelectric phase (BST) and low losses dielectric material (MgO, $MgAl_2O_4$, or Mg_2TiO_4) [6,8,9] leading to multi-materials with an adjustable permittivity value and tunability [10,11]. For these ceramic/ceramic composites (BST/ceramic), many interdiffusion problems were encountered when conventional solid state methods were used leading to modifications of the structural properties and a shift of the Curie temperature [6,11–14]. To prevent these issues, the preparation step is decisive and Spark Plasma Sintering (SPS) thanks to the fast kinetics it allows, is efficient in preventing chemical reaction between the two phases and yields highly densified composites at lower temperatures and much shorter holding times compared to conventional sintering [15,16].

As seen in previous works, the pressure used during SPS is a determining parameter which can lead in some cases to a microstructure anisotropy due to inclusion deformation perpendicularly to the stress applied [17]. Some authors have already published on the *in-situ* texturation of lamellar or acicular compounds via this uniaxial pressure leading to oriented or anisotropic microstructures [18,19] but to the best of our knowledge there are no examples of controlling inclusion shape in composites by SPS. Here, we propose to study the impact of MgO inclusion morphology on the sintering of composites and on their properties. Two types of dielectric inclusions are mixed with the $BaTiO_3$ (BT) matrix: (i) powder from atomization with nanosized grains largely agglomerated in pseudospherical granules of a few tens of microns; (ii) same powder from atomization thermally treated at high temperature in order to increase the mechanical resistance of the granules. Accurate control of both precursor preparation and sintering processes provides the advantage of the pressure

* Corresponding author at: CNRS, Institut Carnot Cirimat, 118 route de Narbonne, F-31062 Toulouse, France.
E-mail address: estournes@chimie.ups-tlse.fr (C. Estournès).

http://dx.doi.org/10.1016/j.scriptamat.2015.08.006
1359-6462/

applied during SPS to deform the inclusions (or not) and thus to tune the dielectric properties of the composites.

In the present study, microstructural and dielectric characteristics are compared for pure $BaTiO_3$ and three-dimensional random composites made of $BaTiO_3$ and a small amount of MgO (4 wt%). BT particles (mean diameter close to 300 nm) were purchased from (Sakai Chemical Industry Co., Japan). MgO powders (97%) were supplied by Merck (Darmstadt, Germany) and are made of spheroidal spray-dried soft granules (≈30 μm) (Fig. 1A). Each of them is composed of nanometric elementary crystallites. MgO granules (4 wt%) were dispersed in a BT matrix, and a mixing step was performed by hand in an agate mortar as described in [17] (BT/MgO). MgO granules were also annealed individually in an inductive furnace at 1600 °C for 2 h (Fig. 1B) and blended with BT powders as well (BT/MgO1600). The strategy was to obtain a set of "rigid" individual MgO granules. The change in morphology compared to non-annealed granules lies mainly in the growth of the elementary particles (from 100 nm to 2 μm) associated with the shrinkage of the aggregates (≈20 μm), clearly observed on FESEM micrographs (Field Emission SEM, JEOL 6700F). To investigate the initial internal microstructure (i.e. BT + MgO powders), 3D-imaging by synchrotron X-ray Computed Micro Tomography (XCMT) were used. The European Synchrotron Radiation Facility (ESRF, Grenoble, France) provides beamlines dedicated to 3D-imaging [20,21]. Experiments were performed at the ID-19 beamline, in "Pink Beam" conditions [22,23]. The energy was equal to 37 keV and the pixel size was set to 0.28 μm. The field of view was 573 × 573 μm. In order to investigate, in 3D, the initial microstructure, mixed powders were consolidated by PMMA [17]. 3D-imaging of non-annealed MgO reveals the complex porous structure of the granules (Fig. 1C). Pores, at least the largest (pore size > 500 nm), appear to be mainly located on the shell of the granule, and their volume fraction can range from 7% to 15%, depending on the granules. A smaller kind of porosity (<500 nm) can be observed as well, reflecting local variations of the dark gray levels inside the granules. MgO annealed at 1600 °C was not imaged within the BT matrix, but simply loaded onto glass capillary tubes (Fig. 1D). The global porosity was also calculated, with an average value of 19%. Annealed MgO granules appear to be highly densified right to the core of the granule. Compared to initial powders nano porosities tended to disappear to the benefit of well-defined micro porosities.

All samples were sintered using a Dr. Sinter 2080 SPS apparatus (SPS Syntex Inc., Japan) of the *Plateforme Nationale de Frittage Flash* located at the Université de Toulouse III Paul Sabatier. The mixed BT and MgO powders were loaded onto an 8 mm inner diameter graphite die. The temperature was automatically raised to 600 °C over a period of 3 min and then, monitored and regulated by an optical pyrometer. A heating rate (100 °C/min) was used to reach the final temperature (1100 °C). Uniaxial pressure (50 MPa) was applied during the heating. Pure BT ceramic was sintered in the same conditions. After sintering, all the ceramics were reoxidized during post-treatment performed in air at 800 °C for 10 h in order to reduce the concentration of oxygen vacancies originating from the low oxygen partial pressure applied during the SPS process, and to remove carbon contamination and release residual strain.

Microstructure and morphology analysis of the composites were recorded using the FESEM on the polished surface (Fig. 2). First of all, ceramics present very high density and only a few pores are visible on these pictures. Experimental densities measured by Archimedes' method on BT and BT/MgO ceramics were similar and higher than 99%. For BT/MgO1600, the density was lower (95%) due to residual porosity observed in MgO inclusions (Fig. 2D). The disk-shaped inclusions revealed as MgO by energy

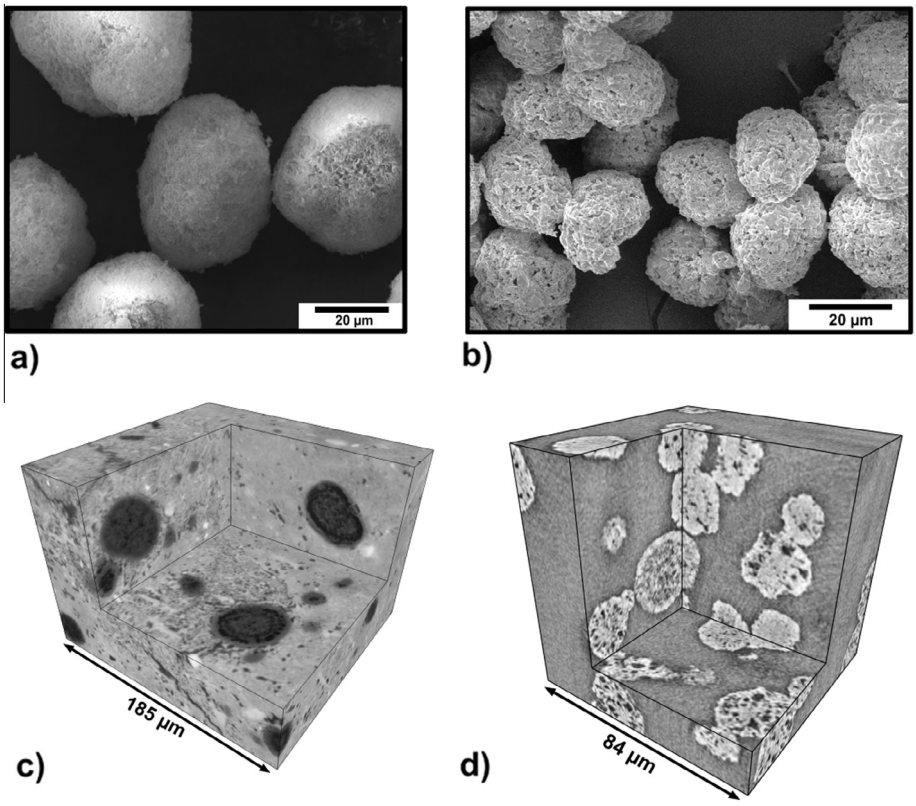

Fig. 1. MgO granules observed by SEM and XCMT. (a) SEM image of MgO granules sorted at ≈30 μm diameter. (b) SEM image of MgO granules annealed at 1600 °C. (c) Multiple cross-section images of the initial microstructure of BT–MgO composite obtained by XCMT. MgO are in dark gray levels and the BT matrix is in light gray. (d) MgO granules annealed at 1600 °C. Particles were loaded into glass capillary tubes.

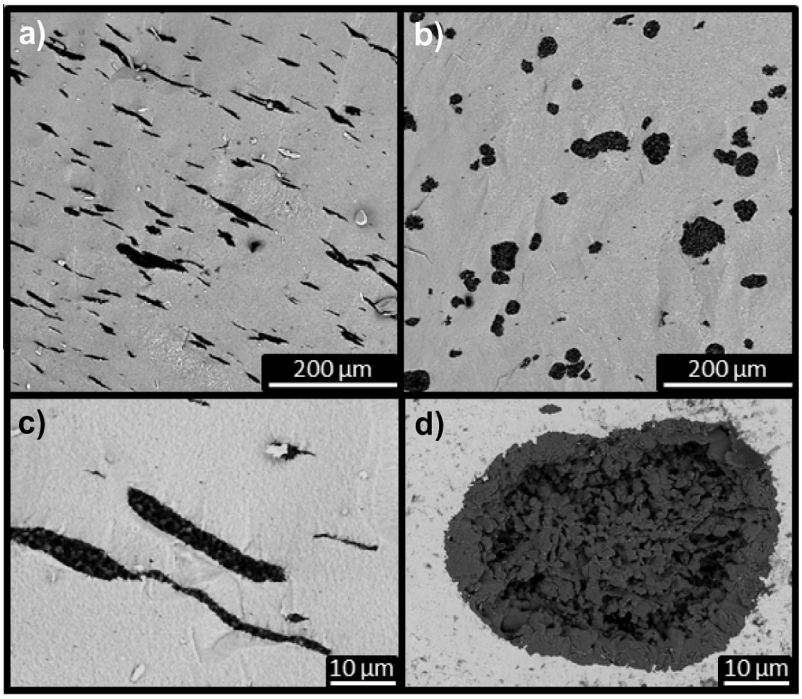

Fig. 2. FESEM micrographs of the polished surface of BT/MgO (left) and BT/MgO1600 (right) composites sintered by SPS.

dispersive analysis (appears in black in back scattered images) were randomly dispersed through the matrix. For BT/MgO (Fig. 2A and C), the deformation of the non-annealed MgO inclusions resulted from the uniaxial pressure applied during the sintering. Both the soft plastic behavior of MgO nanoparticles and grain rearrangement by sliding and/or shearing at the matrix/inclusion interfaces can explain such accommodation. The aspect ratio of the inclusions (length/thickness) statistically calculated using SEM images was equal to 6.0 and characteristic of anisotropic objects (rods, wires or fibers) [24]. Compared to the initial granules, the porosity within the inclusions was diminished and the particle size increased up to 600 nm stemming from MgO densification despite the low sintering temperature used (1100 °C) here compared to that used in natural sintering (1600 °C) [25]. Consequently the deformation of inclusions can be associated with sintering phenomena.

Annealing MgO powder at different temperatures led to the consolidation of the granules. Thus, depending on their rigidity and the stress applied they were deformed to varying degrees during SPS leading to inclusions with different shapes. Once annealed at 1600 °C, the initial granules are strong enough to sustain the pressure and then maintain their spherical shape within the final ceramic. The applied pressure during sintering no longer led to the deformation previously observed (Fig. 2B and D). The inclusions were randomly dispersed through the matrix. The aspect ratio was estimated at 1.5, a value close to that of a perfect isotropic material [24]. The initial spheroidal shape of rigid MgO granules is conserved after SPS sintering. When considering the biggest inclusions, the internal core structure does not change in terms of particle size (1 µm) and pore distribution. Otherwise, significant growth (up to 3 µm) of the grains located on the shells was observed. The applied stress is relaxed by the grain growth on the shell of the inclusions. As a result the core of the granule remains inert regarding sintering.

It is worth noting that increasing the rigidity of the MgO inclusions did not modify the interfaces, which remained chemically sharp. Dense composites were obtained without any traces of delamination or cracks. Moreover, the grain size of the BT matrix was not affected by the microstructural changes of the MgO inclusions. In both cases, it remained around 300 nm and no exaggerated grain growth was observed on the micrographs confirming the benefits of SPS sintering.

The speed of shrinkage recorded during SPS sintering for the three samples: pure BT, BT/MgO and BT/MgO1600 is reported in Fig. 3. It is surprising to note that no differences are observed between the ceramic without inclusions and the one with the "hard" granules of MgO. In the literature, all studies related to sintering of composites with rigid particles report a long retard in densification and a diminution of sintering kinetics [2,25–28]. This delay, assigned to the inclusion/matrix contacts harmful for sintering, becomes even longer as the volume fraction of inclusions increases and they are small sized (increase of contact number)

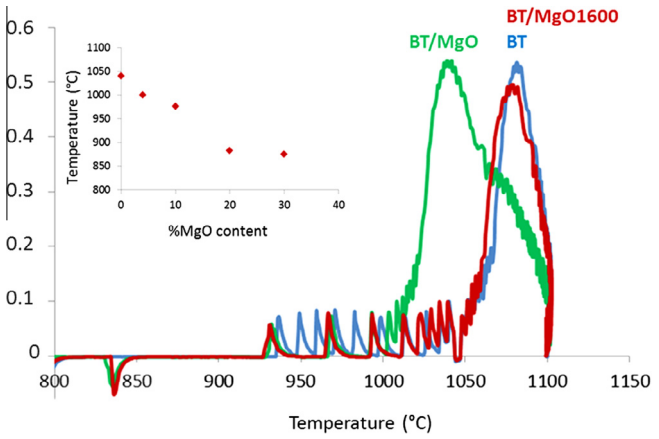

Fig. 3. Speed of shrinkage recorded during SPS sintering of BT (blue), BT/MgO (green) and BT/MgO1600 (red) composites versus temperature. Insert: onset of displacement for BT/MgO composites versus the MgO content. (For interpretation of the references to color in this figure legend, the reader is referred to the web version of this article.)

[27,29]. This results from the shrinkage incompatibilities between the matrix and the inclusions during densification and leads to a decrease of densification rates [30]. Nevertheless, in our case, despite their rigidity, the inclusions do not seem to impact the sintering kinetics, possibly due to the small quantity of MgO (4 wt%) and/or the small size of $BaTiO_3$ grains, which allows rearrangement and the densification near the inclusions. Even with hard spheres of 15 μm, no pores were observed in the matrix (Fig. 2B).

On the other hand, for the BT/MgO composite, the onset of densification occurred at lower temperatures compared to pure BT ceramic (−100 °C for 4 wt% of MgO). This tendency is confirmed when the MgO content is increased (up to 30 wt%) as shown in the inset Fig. 3. The more MgO is added into the composite, the earlier the densification occurs. Thus, the deformation of the inclusions accelerates the sintering rates in the early stages of the SPS process. As previously mentioned, such behavior is unusual for the sintering of composites with inclusions (usually rigid and chemically inert). Here, the inclusions can be considered inert because no interdiffusion or reaction occurs between the two phases as pointed out above (Fig. 2). Furthermore, no interaction was observed for the "hard" inclusions; MgO does not play the role of a sintering aid. The start of shrinkage at lower temperatures is due to the grain rearrangement by sliding and/or shearing at the matrix/inclusion interfaces. This reorganization is favored by the uniaxial pressure used during SPS process, which leads to the collapse and the orientation of inclusions perpendicularly to the load applied and to the microstructural anisotropy. Moreover, this deformation favors the sintering of inclusions. This is supported by the MgO grain growth observed at a sintering temperature as low as 1100 °C. These results can be compared to the work of Yoon et al. who prepared $BaTiO_3$–Cu composites by SPS [3]. In their work, the copper ductility at low temperature (~400 °C) associated to the applied pressure led to the acceleration of sintering during matrix rearrangement. They also observed the deformation of Cu particles in the BT phase perpendicularly to the pressure.

Dielectric measurements were performed using a Wayne-Kerr component analyzer 6425 in the temperature and frequency ranges 200–500 K and 100 Hz–100 kHz respectively. Gold electrodes were deposited on two parallel faces of the ceramic. The real part of the permittivity derived from the capacitance was measured directly. The Curie temperature occurring at 398 K for pure BT did not shift when MgO was added to the ferroelectric matrix (whatever the inclusion shape) confirming both the absence of interdiffusion and the quality of the interfaces between the two components. As expected, the dielectric phase lowered the permittivity values compared to BT (Fig. 4). A reliable comparison of the permittivity values can be made as all the ceramics have comparable densities (>97%). It can be noted that the geometry of the inclusions has a strong impact not only on the effective permittivity of the composite but also on the overall dielectric behavior at the different phase transitions. The dielectric response of the composite with flattened inclusions exhibits a broad permittivity peak in the vicinity of the cubic-tetragonal transition. The permittivity was lowered compared to BT free of dielectric inclusions over the entire temperature range investigated. Such a decrease associated with the broadening of the dielectric anomaly leads to a significant thermal stabilization of permittivity. When the ferroelectric matrix contained spheroidal inclusions, a more classic dielectric behavior was restored with, in particular, permittivity values at the orthorhombic–tetragonal transition much lower than at T_C. The dielectric anomaly was sharp similar to that of BT. The most striking result lies in the possibility to tune the overall dielectric behavior of BT/MgO composites simply by changing the microgeometry of the inclusions. Deeper investigations are required to understand the link between the inclusion deformation and the resulting matrix properties.

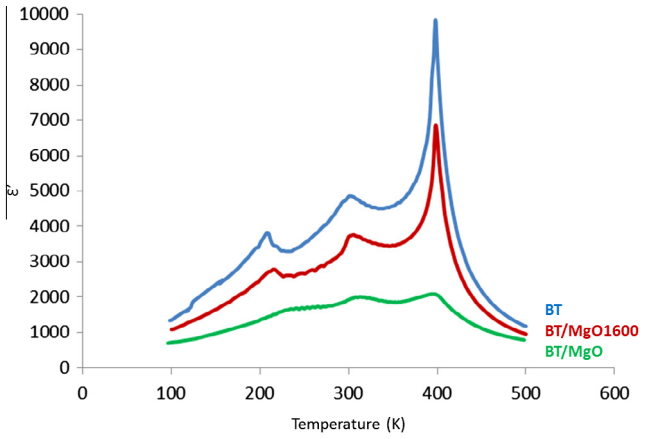

Fig. 4. Dielectric permittivity vs temperature of BT (blue), BT/MgO (green) and BT/MgO1600 (red) composites sintered by SPS. All data were obtained at 10 kHz. (For interpretation of the references to color in this figure legend, the reader is referred to the web version of this article.)

We demonstrated that SPS sintering is a suitable technique for obtaining fully dense BT/MgO composites whatever the mechanical properties of the dielectric inclusions. A reliable comparison of composites with similar density, quality of interfaces and phase content was thus possible. The adjustable parameter here was the morphology of the inclusions, which can be controlled either by prior annealing to obtain hard inclusions or by sintering pressure to deform the initially soft MgO inclusions. The first noticeable effect is the densification gain from the deformation of the soft inclusions during the early stages of sintering. The second noteworthy result is the possibility to adjust the permittivity simply by changing the morphology of the MgO inclusions. We have demonstrated here that controlling the mechanical properties and geometry of the inclusions within a functional matrix opens new insights for the control of both sintering and the resulting properties.

Acknowledgements

This work has been made possible by the financial support of the ANR project ARCHIFUN (ANR-12-BS08-009). Electron microscopy was performed at the "Centre de microcaractérisation Raimond Castaing" – UMS 3623). We acknowledge the European Synchrotron Radiation Facility (ESRF) for provision of synchrotron radiation facilities, in particular the ID19 team for the technical support during the experiments.

References

[1] V. Viswanathan, T. Laha, K. Balani, A. Agarwal, S. Seal, Mater. Sci. Eng. R Rep. 54 (2006) 121–285.
[2] S. Yoon, C. Pithan, R. Waser, J. Dornseiffer, Y. Xiong, D. Grüner, Z. Shen, S. Iwaya, J. Am. Ceram. Soc. 93 (2010) 4075–4080.
[3] S. Yoon, J. Dornseiffer, Y. Xiong, D. Grüner, Z. Shen, S. Iwaya, C. Pithan, R. Waser, J. Eur. Ceram. Soc. 31 (2011) 773–782.
[4] P. Kim, S.C. Jones, P.J. Hotchkiss, J.N. Haddock, B. Kippelen, S.R. Marder, J.W. Perry, Adv. Mater. 19 (2007) 1001–1005.
[5] T. Hu, J. Juuti, H. Jantunen, T. Vilkman, J. Eur. Ceram. Soc. 27 (2007) 3997–4001.
[6] K.W. Plessner, R. West, J. Electron. Control 4 (1958) 51–57.
[7] P. Liu, J. Ma, L. Meng, J. Li, L. Ding, J. Wang, H.-W. Zhang, Mater. Chem. Phys. 114 (2009) 624–628.
[8] J. Zhang, J. Zhai, X. Chou, X. Yao, J. Am. Ceram. Soc. 91 (2008) 3258–3262.
[9] L.C. Sengupta, S. Sengupta, Mater. Res. Innov. 2 (1999) 278–282.
[10] W. Chang, L. Sengupta, J. Appl. Phys. 92 (2002) 3941–3946.
[11] P. Baxter, N.J. Hellicar, B. Lewis, J. Am. Ceram. Soc. 42 (1959) 465–470.
[12] B. Su, T.W. Button, J. Appl. Phys. 95 (2004) 1382–1385.
[13] M. Zhang, J. Zhai, B. Shen, X. Yao, J. Am. Ceram. Soc. 94 (2011) 3883–3888.
[14] C. Elissalde, M. Maglione, C. Estournes, J. Am. Ceram. Soc. 90 (2007) 973–976.
[15] U.-C. Chung, C. Elissalde, M. Maglione, C. Estournès, M. Paté, J.P. Ganne, Appl. Phys. Lett. 92 (2008) 042902.

[16] J. Lesseur, D. Bernard, U.-C. Chung, C. Estournès, M. Maglione, C. Elissalde, J. Eur. Ceram. Soc. 35 (2015) 337–345.
[17] J.G. Noudem, D. Kenfaui, D. Chateigner, M. Gomina, Scr. Mater. 66 (2012) 258–260.
[18] J. Liu, Z. Shen, M. Nygren, Y. Kan, P. Wang, J. Eur. Ceram. Soc. 26 (2006) 3233–3239.
[19] D. Bernard, Ø. Nielsen, L. Salvo, P. Cloetens, Mater. Sci. Eng., A 392 (2005) 112–120.
[20] J.Y. Buffiere, E. Maire, J. Adrien, J.P. Masse, E. Boller, Proc. Soc. Exp. Mech. Inc. 67 (2010) 289–305.
[21] E. Boller, P. Tafforeau, W. Ludwig, L. Helfen, L. Salvo, P. Cloetens, E. Boller, P. Tafforeau, W. Ludwig, L. Helfen, T. Weitkamp, Matér. (2010). 2010 Oct 2010 Nantes Fr.
[22] M. Renier, P. Bernard, W. Van De Vijver, K. Smets, P. Tafforeau, J. Phys: Conf. Ser. 425 (2013) 212008.
[23] J. Besson, Mech. Mater. 19 (1995) 103–117.
[24] G.S. Upadhyaya, Sintered Metallic and Ceramic Materials, J. Wiley and Sons, New York, 2000.
[25] O. Sudre, F.F. Lange, J. Am. Ceram. Soc. 75 (1992) 519–524.
[26] Y. Nakada, T. Kimura, J. Am. Ceram. Soc. 80 (1997) 401–406.
[27] Z. Yan, C.L. Martin, O. Guillon, D. Bouvard, Scr. Mater. 69 (2013) 327–330.
[28] L. Olmos, C.L. Martin, D. Bouvard, Powder Technol. 190 (2009) 134–140.
[29] C. Wang, S. Chen, Sci. China Phys. Mech. Astron. 55 (2012) 1051–1058.
[30] M.W. Weiser, L.C. De Jonghe, J. Am. Ceram. Soc. 71 (1988) C125–C127.